Letter

Elastic computational metasurfaces for subwavelength differentiations

Guangyuan Su,[1] Zongliang Du,[2] and Yongquan Liu[1,*]

[1]*State Key Laboratory for Strength and Vibration of Mechanical Structures, School of Aerospace Engineering, Xi'an Jiaotong University, Xi'an 710049, China*

[2]*State Key Laboratory of Structural Analysis, Optimization and CAE Software for Industrial Equipment, Department of Engineering Mechanics, Dalian University of Technology, Dalian 116023, China*

(Received 28 October 2023; revised 27 January 2024; accepted 29 March 2024; published 15 April 2024)

Analog computations enable information processing with negligible energy costs and massively parallel architectures, but currently are limited to process macroscale waveforms with characteristic lengths much larger than the operating wavelength λ_0. We explore here, in contrast, the differentiation of subwavelength waveforms by using an elastic computational metasurface. We find that the numerical aperture of metasurface governs the threshold of the characteristic length of waveforms, below which the metasurface outputs an identical differentiated pattern. Remarkably, for a subwavelength waveform below the threshold, the metasurface can locate the source because the differentiated pattern is of cylindrical wavefronts centered at the source, which can be harnessed to detect single or multiple subwavelength-scaled scatterers. The detectability reaches a deep subwavelength of $0.12\lambda_0$, and the localization error stays smaller than λ_0. Our work elucidates the physical image of subwavelength differentiations, which may promote promising applications in nondestructive testing, signal processing, and computational acoustics.

DOI: 10.1103/PhysRevB.109.L161108

By avoiding the use of analog-to-digital convertors, analog computations have recently caught substantial attention to exhibit high energy utilization efficiencies and massively parallel computing capabilities [1–5]. Although it has a long history traced back to the Antikythera mechanism in ancient Greece [6], this field is revitalized by the concept of computational metamaterials [3], which can perform complex mathematical operations with subwavelength footprints. To date, computational metamaterials have been extended to various disciplines including optics, electromagnetics, and acoustics [7–20], offering novel avenues towards sound identification, signal processing, and augmented reality [21–23]. It is noted that current computational metamaterials are mostly exploited at the macroscale, where the characteristic lengths of constituent waveforms in input signals are much larger than the wavelength λ_0 [7,9–13,17,18,20]. For example, differentiation metasurfaces have been used to process waveforms with characteristic lengths of dozens of λ_0 [7,9,17]. As exemplified in Fig. 1(a), differential operators lead to drastic changes near where signals suddenly appear/disappear, while differentiating a constant becomes zero elsewhere. As a result, optical differentiation metasurfaces have been exploited to extract the object edges in images with dimensions of at least hundreds of λ_0 [11–13,18]. An all-optical deep learning framework based on multiple layers of diffractive surfaces was developed to perform classifications of centimeter-scale images [20]. However, when the characteristic length of the signal reduces to roughly the wavelength λ_0, it will be hard to do edge detection due to the intermingling of differential signals. For an extreme case, the analog computation of subwavelength input waveforms remains an open question. In fact, this issue is physically fundamental to the resolution limits of devices, which are restricted to the diffraction limit ($\lambda_0/2\mathrm{NA}$, where NA is short for numerical aperture of an imaging system) [24], and definitely plays an important role when analog computation comes into the subwavelength scale.

In contrast, we will explore the possibility and its applications of doing subwavelength differentiation by using an elastic computational metasurface in this Letter. We find that the underlying physics for this operation does not contradict the theory of diffraction limit, where any device cannot distinguish two scatterers (or corresponding wavefronts) closer than it. However, we must emphasize that one is still able to observe the existence (and even the location) of the scatterers below the diffraction limit. As illustrated in Fig. 1(b), the subwavelength differentiations in this Letter are featured by the input waveform with a characteristic length smaller than the diffraction limit $\lambda_0/2\mathrm{NA}$. Considering the subwavelength size of the waveform, we can regard it as a point source to generate the Green's function as the input field. After processing by the computational metasurface, the differential Green's function will still be centered at the point source but with a redistribution in amplitude. Similarly, if the subwavelength waveform is generated by a subwavelength tiny scatterer, the scattering wave field will be centered at the tiny scatterer after analog differentiations. We will prove that, after processing by the computational metasurface, the imperceptible scattering wave becomes conspicuous in amplitude distributions, allowing the detection and localization of the tiny scatterer. We would like to stress that the practical applications of subwavelength analog computations are worth exploration,

*Corresponding author: liuy2018@xjtu.edu.cn

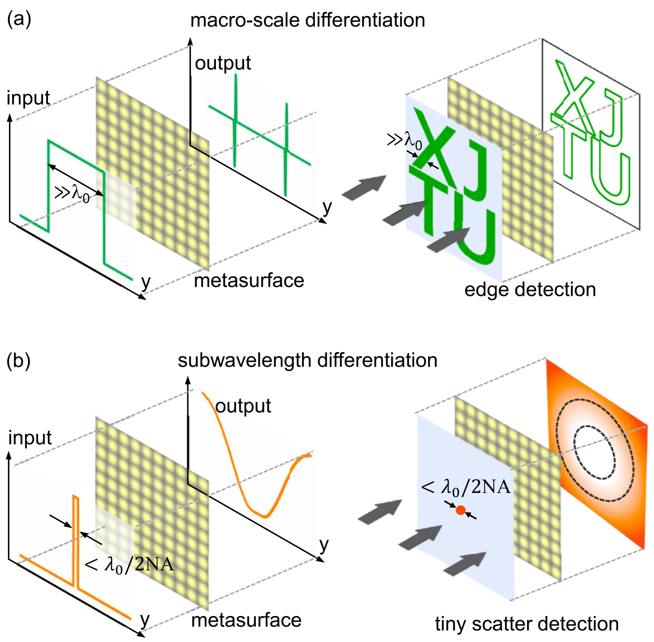

FIG. 1. Macroscale and subwavelength analog differentiations by using metasurfaces. (a) For macro analog differentiation, the characteristic length of the input waveform is much larger than the operating wavelength λ_0. Its typical application is edge detection, where the sizes of scatterers are generally hundreds of λ_0. (b) For subwavelength differentiation, the characteristic length of the input waveform is less than the diffraction limit $\lambda_0/2\mathrm{NA}$. One may find applications in detecting a subwavelength tiny scatterer.

especially in the fields of nondestructive testing or signal processing. Pioneers have harnessed the bandgap-based metamaterials to detect defects through the generated higher harmonic waves, bridging the gap between metamaterials and nondestructive testing [25–27]. Different from those bandgap-based metamaterials, the proposed computational metasurfaces exhibit exotic angular dispersive behaviors, and thereby hopefully bring new insights to nondestructive testing of subwavelength defects. In addition, towards subwavelength detections, the hyperlens technique provides a successful paradigm [28]. Although the hyperlenses can achieve far-field superresolution imaging, they are required to be placed at the near-field proximity of objects to transform the scattered evanescent waves into propagating ones. In contrast, the proposed method is based on the analog differentiations directly to scattered propagating waves, and thereby avoids the overstrict near-field manipulation conditions required by the hyperlens technique and other evanescent wave-based methods [29].

To exemplify our proposal, we first design an elastic metasurface to implement the second-order differentiation to the A_0 mode Lamb waves on a 0.5 mm-thickness plate. For an nth − order spatial differentiation, the transfer function of the metasurface needs to present an angular response of $t(\theta) \propto (ik_y)^n$ [3], where $k_y = k_0 \sin\theta$ is the tangential wave number, with k_0 the wavenumber in free space and θ the direction of the input wave, respectively. For an even-order differentiation, the metasurface should be mirror symmetric along the x direction because of reciprocity [7]. Based on the above considerations, we propose a dual-layer configuration

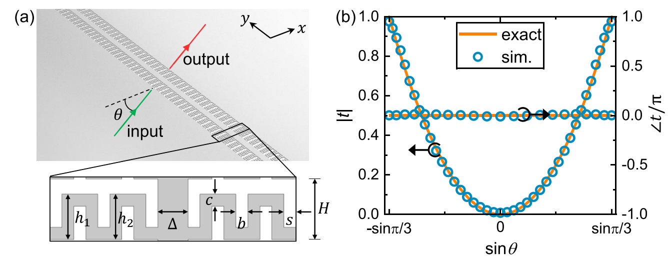

FIG. 2. Elastic computational metasurface for the second-order spatial differentiation. (a) Dual-layer configuration of the metasurface. The enlarged view shows the unit cell, which consists of only one cascaded zigzag subunit. (b) Transmitted amplitude $|t|$ and phases $\angle t$ of the optimized metasurfaces. The solid lines are exact values.

of the metasurface with only one symmetric cascaded zigzag subunit, as depicted in Fig. 2(a). The geometric parameters of metasurfaces involve zigzag heights h_1 and h_2, spacings b and s, and interlaminar gap size Δ. In order to ensure the purity of the output waves, we design the metasurface so that it can only excite the *zeroth*-order diffracted waves, which requires the lattice constant H to be less than $0.5\lambda_0$ [30]. By tailoring the coupling effect between two layers, one can engineer angular dispersions of the metasurface [31]. Herein, an optimization formulation based on the genetic algorithm is developed to design the metasurfaces (see Supplemental Material [32] for details. As an example, we choose 304 stainless steel as the raw material to design the metasurface plate, with Young's modulus 200 GPa, mass density 7900 kg/m^3, and Poisson's ratio 0.3, respectively. The wavelength λ_0 is thus 10.3 mm at the operating frequency 40 kHz. The optimized metasurface consists of two cascaded sublayers with thicknesses less than $0.7\lambda_0$, and thus shows a much more compact configuration than current computational devices based on bulky Fourier transforming systems [8,9]. Figure 2(b) presents the transmitted amplitudes $|t|$ and phases $\angle t$ of the designed metasurface, which exhibit a perfect agreement with the exact values (solid lines). For the passive metasurfaces in this work, the exact angular responses for the second-order differential function should be $t(\theta) = \eta(ik_0 \sin\theta)^2$, where η is a factor normalizing the amplitude transmission. The phase responses are constant with variations of $\sin\theta$, because the sign of $t(\theta)$ stays fixed. By considering a full transmission at the NA point that $|t_{\mathrm{NA}}| = 1 = \eta k_0^2 \mathrm{NA}^2$, the scaling factor η is determined to be $1/k_0^2\mathrm{NA}^2$. As a result, the exact amplitude responses $|t(\theta)| = (\sin\theta/\mathrm{NA})^2$ can be obtained. The NA of the proposed metasurface reaches $\sin\pi/3$, corresponding to a resolution limit of $\lambda_0/2\mathrm{NA} = 0.58\lambda_0$. This value defines the threshold of characteristic lengths of waveforms, below which the length information is lost by metasurfaces due to the Abbe's limit of diffraction for an optical lens [24]. This is in contrast with the macroscale analog differentiation that is almost immune from the effect of device resolutions. In Supplemental Material [32], we further design a first-order differentiation metasurface, also with $\mathrm{NA} = \sin\pi/3$, confirming the robustness of the proposed design paradigm. It is noted that the mirror symmetry along the x direction is broken for an odd-order differentiation, which may lead to a more complex configuration of the unit cell.

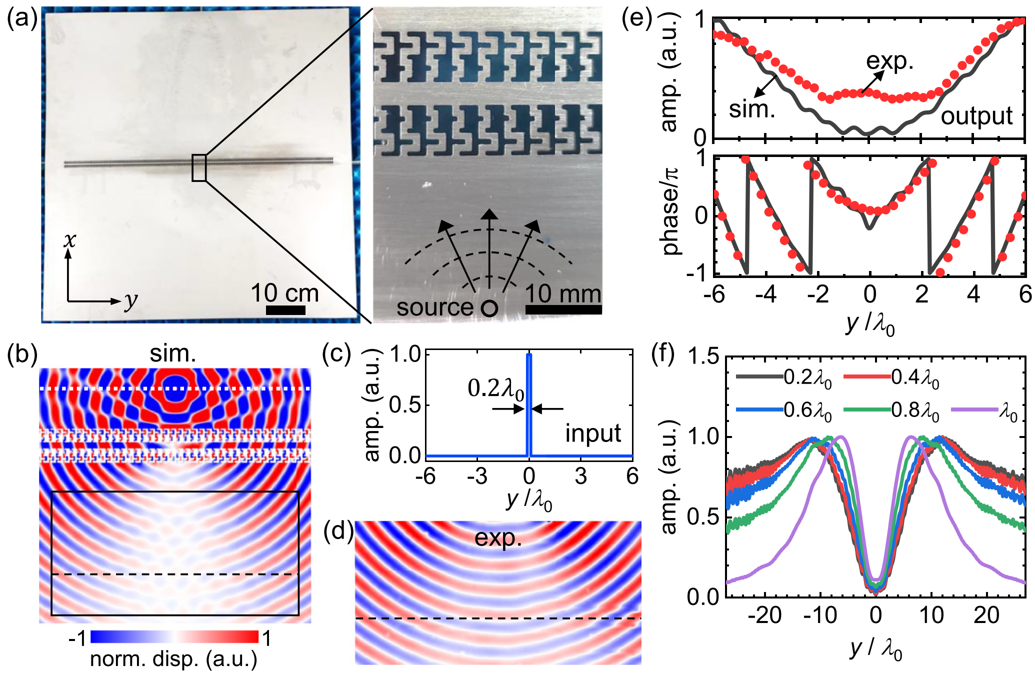

FIG. 3. Subwavelength differentiation by using an elastic computational metasurface. (a) Photograph of the fabricated elastic computational metasurface. The enlarged view shows that the point source is placed ahead of the metasurface along its middle line at a distance of $2\lambda_0$. (b) Simulated output wave field under illumination of the input signal in (c) impinges on the metasurface. The characteristic length of incident waveform is $0.2\lambda_0$. (d) The tested wave field for a point source to stimulate the input waveform. The solid box marks the region for experimental measuring. (e) Output amplitude and phase distributions on the dashed lines in (b) and (d) that are behind the metasurface at a distance of $5\lambda_0$. (f) Output amplitude profiles with different characteristic lengths of the input waveforms ranging from $0.2\lambda_0$ to λ_0. Note that (b) and (d) display the out-of-plane displacement fields that are normalized by the maximal magnitudes of differentiated waves.

The elastic computational metasurface is then fabricated by wire cutting technology, as shown in Fig. 3(a). The thickness of the dual-layer metasurface is 16.8 mm and the period of the unit cell is $H = 3.5$ mm. Figure 3(b) presents the simulated wave field for the elastic computational metasurface under illumination of the input signal in Fig. 3(c), where the characteristic length of the input waveform is $0.2\lambda_0$. It is clear that the output wave patterns are centered at the source, with amplitudes decreasing from both sides to the middle area. In fact, such a subwavelength waveform excites a cylindrical wave field, and thereby can be approximated by a point source (see Supplemental Material [32] for details). As a verification, we put a piezoelectric patch as a point source ahead of the metasurface along its middle line at a distance of $2\lambda_0$, as shown by the enlarged view in Fig. 3(a). The output wave field is experimentally measured by using a laser Doppler vibrometer (NLV-2500, Polytec). As expected, a cylindrical-like wave field centered at the point source but with obvious amplification along with the distance from the middle line is observed in Fig. 3(d). For quantitative comparison, the output amplitude and phase distributions on the dashed lines in Figs. 3(b) and 3(d) are presented in Fig. 3(e), showing excellent agreement with each other. Manufacturing errors result in leaked energy around the middle area (see Supplemental Material for the sensitivity of the performance of metasurfaces to the geometric errors [32]). In Supplemental Material [32], we also provided the output wave pattern processed by a first-order differentiation metasurface. As expected, an asymmetric cylindrical-like wave pattern is observed, with a linear amplification along with the distance from the middle line.

To elucidate the diffraction limit effect of the computational metasurface, we take different characteristic lengths of input waveforms ranging from $0.2\lambda_0$ to λ_0. The output amplitude profiles are displayed in Fig. 3(f). For characteristic lengths less than the resolution limit $0.58\lambda_0$, almost identical output amplitude profiles are obtained, which means that the metasurface cannot distinguish the waveforms in this case. However, the output amplitudes on both sides sharply decrease when the characteristic lengths increase to larger than $0.58\lambda_0$, verifying the resolving capability of the metasurface. In particular, for the case of a large characteristic length of λ_0, the output amplitudes at two sides approach to zero, which implies the output pattern turning into two beams, and thereby confirms the edge extraction of macroscale wavefronts [9–13,17,18]. In Supplemental Material, we determine the maximal sampling distance for the data in Fig. 3(f) [32].

It is noteworthy that for an input waveform with a characteristic length smaller than the resolution limit, the differentiated waves still carry the location information of the input source, allowing the detection and localization of a subwavelength tiny scatterer. Figure 4(a) illustrates the proposed detection principle. For a plane wave $w_p = A_p e^{ik_0 x}$ impinging on a subwavelength scatterer, the scattering wave w_s is in the form of wave expansion and can be approximated by the zeroth-order term in the far field, which corresponds to

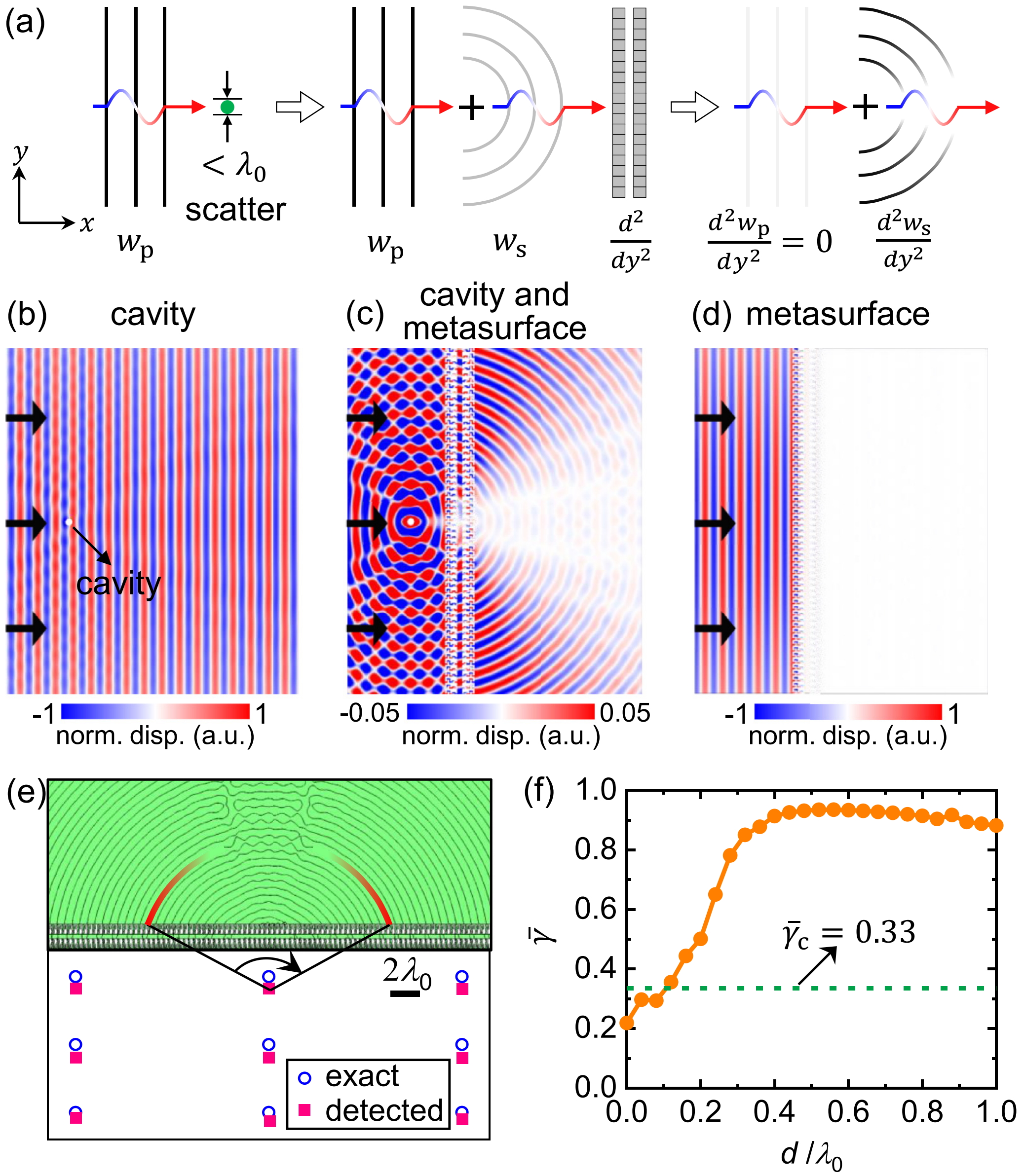

FIG. 4. Subwavelength scatterer detection and localization by using a computational metasurface. (a) Schematic of the detection principle. (b) Simulated plane wave field perturbed by a subwavelength circular cavity with diameter $d = 0.4\,\lambda_0$. (c) The counterpart of (b) with an elastic computational metasurface behind the cavity at a distance of $2\lambda_0$. (d) Simulated resulted wave field for the metasurface filtering out the incident plane wave. (e) Localization of cavities at different positions. (f) Variations of the scattering cross section $\bar{\gamma}$ with the cavity diameter d. Note that (b)–(d) display the out-of-plane displacement fields normalized by the magnitudes of incident waves. To clearly display the differentiated scattered waves, the scale of (c) is decreased to ± 0.05.

a cylindrical wave [33],

$$w_s = A_s H_0^{(1)}(k_0 r), \tag{1}$$

where $H_0^{(1)}$ is the zeroth-order Hankel function of the first kind, $r = \sqrt{(x - x_s)^2 + (y - y_s)^2}$ with (x_s, y_s) the coordinate of the scatterer. The subwavelength scatterer is generally undetectable, because the amplitude of the scattering wave is much smaller than that of the incident wave $A_s \ll A_p$. Figure 4(b) shows a plane wave field under the disturbance of a subwavelength circular cavity with diameter $d = 0.4\lambda_0$. One can see that the plane wave field is barely distorted. However, after the operation of the second-order differentiation, the incident wave w_p can be filtered out by $\partial^2 w_p/\partial y^2 = 0$. Meanwhile, the differentiated scattering wave becomes

$$\frac{\partial^2 w_s}{\partial y^2} = \frac{1}{2} k_0^2 \sin^2\alpha A_s \big(H_2^{(1)}(k_0 r) - H_0^{(1)}(k_0 r)\big) - \cos^2\alpha A_s \frac{k_0}{r} H_1^{(1)}(k_0 r), \tag{2}$$

where α is the central angle with respect to the scatterer and $H_2^{(1)}$ is the second-order Hankel function of the first kind. In the far-field region where $k_0 r \gg 1$, it can be deduced that $\partial^2 w_s/\partial y^2 \cong k_0^2 \sin^2\alpha\, w_s$, which means that the amplitudes of scattering waves are redistributed through a factor of $k_0^2 \sin^2\alpha$.

As shown in Fig. 4(c), if one places the computational metasurface behind the tiny scatterer (at a distance of $2\lambda_0$, for example), cylindrical-like transmitted wavefronts will be observed with significantly increased amplitudes along with the central angle α. Figure 4(d) provides the numerical verification of filtering out an incident plane wave by using the computational metasurface. The stark contrast between the wave patterns in Figs. 4(b) and 4(c) confirms the proposed principle to detect a subwavelength scatterer. In Supplemental Material [32], we further verify the robustness of this principle by detecting a cavity near the metasurface edge and by detecting a subwavelength cylinder glued on the plate as a tiny scatterer.

Considering that Eq. (2) exhibits a circular isophase contour centered at the scatterer, we can further localize it by reversing the center of the output wavefronts (see Supplemental Material [32] for details). As exemplified in Fig. 4(e), we position subwavelength cavities at different locations. The largest distance between the cavity and the elastic computational metasurface in Fig. 4(e) reaches up to $12\lambda_0$, ensuring its far-field testability of the proposed method. The localization error, defined as the distance between the detected location (solid square) and the exact one (hollow circle), stays smaller than one wavelength. For the metasurface length of 700 mm and cavity diameter of $0.4\lambda_0$ in Fig. 4(e), we can obtain that the maximal detectable distance between the scatterer and metasurface, $D_{\max} = 202.1$ mm ($\sim 19.6\lambda_0$) (see the Supplemental Material for detailed analyses on $D_{\max}$ [32]). To further investigate the detectivity of the metasurface, we define the scattering cross section as $\bar{\gamma} = \frac{1}{N}\sum_{j=1}^{N}\gamma_j$, where $\gamma_j = (|w|_{\max,j} - |w|_{\min,j})/(|w|_{\max,j} + |w|_{\min,j})$, $|w|_{\max,j}$ and $|w|_{\min,j}$ are the maximal and minimal amplitudes on a wavefront numbered by j, and N is the number of wavefronts for calculation, respectively [34]. Apparently, the condition that $\bar{\gamma} \to 0$ corresponds to a nearly perfect plane wave field, whereas $\bar{\gamma} \to 1$ indicates drastically distorted wave fields due to the existence of the scatterer. Figure 4(f) displays the simulated $\bar{\gamma}$ as a function of the diameter of the cavity d. The distance between the scatterer and the elastic metasurface is fixed as $2\lambda_0$, and five isophase output wavefronts ($N = 5$) are used here. An over-small scatterer cannot be detected as expected, corresponding to a low value of $\bar{\gamma}$. Meanwhile, one can see that $\bar{\gamma}$ rapidly increases with the diameter d and then comes into a plateau, which verifies the detectability of the scatterer. To intuitively show the effect of scatterer size, the output wave fields for cavity diameters of $0.04\lambda_0$, $0.12\lambda_0$, and 0.60 λ_0 are provided in Supplemental Material [32]. We calculate the wave field for a cavity with diameter $d = \lambda_0$ without the metasurface [32] and take the corresponding scattering cross section as the critical value ($\bar{\gamma}_c = 0.33$). Based on this value, it is found that the detectability of the metasurface reaches a deep subwavelength to $0.12\lambda_0$. In Supplemental Material, we demonstrate the localizations on a Mie-type subwavelength scatterer [32]. The detections on multiple scatterers are also demonstrated by replacing the incident plane waves by beam scans [32]. For experimental verification, the machining accuracy cannot meet the requirement for detections on a scatterer. Detailed analyses are given in Supplemental Material [32]. Experimental verification is expected in the future at larger operating wavelengths to enhance the fabrication tolerance of designed metasurfaces. Furthermore, the proposed method can be extended to other classic waves because the subwavelength differentiation, which is the kernel of the proposed detecting method, is generic. Specifically, the subwavelength differentiation is implemented to the propagating components of flexural waves and is irrelevant to the evanescent components. In this condition, the differential equation for flexural waves $(\nabla^4 - k^4)w = 0$ can be approximated as the Helmholtz equation $(\nabla^2 + k^2)w = 0$ [35]. Hence, the subwavelength differentiations and the proposed detecting method can be extended to other classic waves governed by the Helmholtz equation, such as acoustic and optical waves.

In conclusion, we have explored the possibility of doing subwavelength differentiation by using an elastic computational metasurface, and then proposed its application in detecting tiny scatterers by harnessing the subwavelength differentiation to filter out incident waves and to amplify the scattered waves. For subwavelength circular cavities, the detectable sizes reach deep subwavelength ($0.12\lambda_0$), and the localization error remains smaller than λ_0. The detection method works for cases with multiple scatterers. Our work uncovers the fundamental differences between macroscale and subwavelength differentiations, and provides avenues to the design of high-Q devices with preferable compactness for nondestructive testing and signal processing.

This work was supported by the National Science Foundation of China (Grants No. 12172271 and No. 12372122).

[1] F. Zangeneh-Nejad, D. L. Sounas, A. Alù, and R. Fleury, Analogue computing with metamaterials, Nat. Mater. Rev. **6**, 207 (2021).

[2] A. Cordaro, B. Edwards, V. Nikkhah, A. Alù, N. Engheta, and A. Polman, Solving integral equations in free space with inverse-designed ultrathin optical metagratings, Nat. Nanotechnol. **18**, 365 (2023).

[3] A. Silva, F. Monticone, G. Castaldi, V. Galdi, A. Alù, and N. Engheta, Performing mathematical operations with metamaterials, Science **343**, 160 (2014).

[4] K. Shastri and F. Monticone, Nonlocal flat optics, Nat. Photon. **17**, 36 (2023).

[5] N. M. Estakhri, B. Edwards, and N. Engheta, Inverse-designed metastructures that solve equations, Science **363**, 1333 (2019).

[6] D. de Solla Price, Gears from the Greeks. The mechanism: A calendar computer from ca. 80 B. C., Trans. Am. Philos. Soc. **64**, 31 (1974).

[7] H. Kwon, D. Sounas, A. Cordaro, A. Polman, and A. Alù, Nonlocal metasurfaces for optical signal processing, Phys. Rev. Lett. **121**, 173004 (2018).

[8] S. Y. Zuo, Q. Wei, Y. Cheng, and X. J. Liu, Mathematical operations for acoustic signals based on layered labyrinthine metasurfaces, Appl. Phys. Lett. **110**, 011904 (2017).

[9] S. Y. Zuo, Y. Tian, Q. Wei, Y. Cheng, and X. J. Liu, Acoustic analog computing based on a reflective metasurface with decoupled modulation of phase and amplitude, J. Appl. Phys. **123**, 091704 (2018).
[10] A. Cordaro, H. Kwon, D. Sounas, A. F. Koenderink, A. Alù, and A. Polman, High-index dielectric metasurfaces performing mathematical operations, Nano Lett. **19**, 8418 (2019).
[11] Y. Zhou, H. Zheng, I. I. Kravchenko, and J. Valentine, Flat optics for image differentiation, Nat. Photon. **14**, 316 (2020).
[12] C. Guo, M. Xiao, M. Minkov, Y. Shi, and S. Fan, Photonic crystal slab Laplace operator for image differentiation, Optica **5**, 251 (2018).
[13] T. Zhu, Y. Zhou, Y. Lou, H. Ye, M. Qiu, Z. Ruan, and S. Fan, Plasmonic computing of spatial differentiation, Nat. Commun. **8**, 15391 (2017).
[14] C. Guo, M. Xiao, M. Minkov, Y. Shi, and S. Fan, Isotropic wavevector domain image filters by a photonic crystal slab device, J. Opt. Soc. Am. A **35**, 1685 (2018).
[15] O. Y. Long, C. Guo, W. Jin, and S. Fan, Polarization-independent isotropic nonlocal metasurfaces with wavelength-controlled functionality, Phys. Rev. Appl. **17**, 024029 (2022).
[16] L. Wan, D. Pan, S. Yang, W. Zhang, A. A. Potapov, X. Wu, W. Liu, T. Feng, and Z. Li, Optical analog computing of spatial differentiation and edge detection with dielectric metasurfaces, Opt. Lett. **45**, 2070 (2020).
[17] H. Kwon, A. Cordaro, D. Sounas, A. Polman, and A. Alù, Dual-polarization analog 2D image processing with nonlocal metasurfaces, ACS Photon. **7**, 1799 (2020).
[18] J. Zhou, H. Qian, C. F. Chen, J. Zhao, G. Li, Q. Wu, H. Luo, S. Wen, and Z. Liu, Optical edge detection based on high-efficiency dielectric metasurface, Proc. Natl. Acad. Sci. USA **116**, 11137 (2019).
[19] Y. Shen, N. C. Harris, S. Skirlo, M. Prabhu, T. Baehr-Jones, M. Hochberg, X. Sun, S. Zhao, H. Larochelle, D. Englund, and M. Soljačić, Deep learning with coherent nanophotonic circuits, Nat. Photon. **11**, 441 (2017).
[20] X. Lin, Y. Rivenson, N. T. Yardimci, M. Veli, Y. Luo, M. Jarrahi, and A. Ozcan, All-optical machine learning using diffractive deep neural networks, Science **361**, 1004 (2018).
[21] T. Jiang, C. Li, Q. He, and Z. K. Peng, Randomized resonant metamaterials for single-sensor identification of elastic vibrations, Nat. Commun. **11**, 2353 (2020).
[22] G. Y. Lee, J. Y. Hong, S. Hwang, S. Moon, H. Kang, S. Jeon, H. Kim, J. H. Jeong, and B. Lee, Metasurface eyepiece for augmented reality, Nat. Commun. **9**, 4562 (2018).
[23] F. Zangeneh-Nejad and R. Fleury, Topological analog signal processing, Nat. Commun. **10**, 2058 (2019).
[24] X. Zhang and Z. Liu, Superlenses to overcome the diffraction limit, Nat. Mater. **7**, 435 (2008).
[25] A. S. Gliozzi Miniaci, B. Morvan, A. Krushynska, F. Bosia, M. Scalerandi, and N. M. Pugno, Proof of concept for an ultrasensitive technique to detect and localize sources of elastic nonlinearity using phononic crystals, Phys. Rev. Lett. **118**, 214301 (2017).
[26] S. Gliozzi, M. Miniaci, F. Bosia, N. M. Pugno, and M. Scalerandi, Metamaterials-based sensor to detect and locate nonlinear elastic sources, Appl. Phys. Lett. **107**, 161902 (2015).
[27] A. Mankar Ciampa and A. Marini, Phononic crystal waveguide transducers for nonlinear elastic wave sensing, Sci. Rep. **7**, 14712 (2017).
[28] D. Lu and Z. Liu, Hyperlenses and metalenses for far-field super-resolution imaging, Nat. Commun. **3**, 1205 (2012).
[29] M. Molerón and C. Daraio, Acoustic metamaterial for subwavelength edge detection, Nat. Commun. **6**, 8037 (2015).
[30] Y. Hu, Y. Zhang, G. Su, M. Zhao, B. Li, Y. Liu, and Z. Li, Realization of ultrathin waveguides by elastic metagratings, Commun. Phys. **5**, 62 (2022).
[31] Z. Wang, B. Zhang, and H. Deng, Dispersion engineering for vertical microcavities using subwavelength gratings, Phys. Rev. Lett. **114**, 073601 (2015).
[32] See Supplemental Material at http://link.aps.org/supplemental/10.1103/PhysRevB.109.L161108 for more details on optimization algorithms, numerical and experimental methods, maximal detectable distances, localization method, and detections on multiple scatterers.
[33] Y. H. Pao and C. C. Mow, *Diffraction of Elastic Waves and Dynamic Stress Concentrations* (The Rand Corporation, Santa Monica, 1971).
[34] S. Zhang, C. Xia, and N. Fang, Broadband acoustic cloak for ultrasound waves, Phys. Rev. Lett. **106**, 024301 (2011).
[35] Y. Liu Zhu, Z. Liang, T. Chen, and J. Li, Elastic waves in curved space: Mimicking a wormhole, Phys. Rev. Lett. **121**, 234301 (2018).